Int J Adv Manuf Technol (2017) 89:2675–2689
DOI 10.1007/s00170-016-9379-5

ORIGINAL ARTICLE

A time-space discretization method in milling stability prediction of thin-walled component

Qinghua Song[1] · **Jiahao Shi**[1] · **Zhanqiang Liu**[1] · **Yi Wan**[1]

Received: 28 July 2016 / Accepted: 22 August 2016 / Published online: 29 August 2016

Abstract The stability prediction of thin-walled workpiece milling is an awkward problem due to the time variant of dynamic characteristics during milling process. Integrating the time discretization method for stability prediction mentioned in many articles, a novel time-space discretization method for thin-walled component milling stability prediction is proposed based on thin plate theory and mode superposition principle, which includes the effects of the engagement position between cutter and workpiece and multi-modes of the system. The results show that the method presented is very reliable and efficient, and its accuracy is also in good agreement with experimental results. Additionally, the method can be used to handle various complex boundary conditions by means of the updated Rayleigh-Ritz solutions together with the penalty method. Two case studies are performed to explain the validation of the method as well as milling experiments of a half-clamped thin plate.

Keywords Thin-walled component · Thin plate theory · Time-varying modal parameter · Milling stability · Time-space discretization method

✉ Qinghua Song
ssinghua@sdu.edu.cn

Zhanqiang Liu
melius@sdu.edu.cn

[1] Key Laboratory of High Efficiency and Clean Mechanical Manufacture, Ministry of Education, School of Mechanical Engineering, Shandong University, Jinan, People's Republic of China

1 Introduction

Due to the requirements of high performance products, thin-walled components with complex shape and light weight have become more and more desirable in many application fields, such as military, energy, and aerospace industries. Thin-walled workpiece milling is of great significance [1]. However, high flexibility of the workpiece and the time-varying dynamic characteristics of cutting process are prone to induce severe vibration, which greatly limits the cutting efficiency, damages cutter and spindle units, affects the surface machining quality, and even shortens the service life of a part.

There are many kinds of vibrations in milling process [2], such as free vibration, forced vibration and self-excited vibration, and so on. Regenerative chatter is a kind of self-excited vibration, which has been the research focus in this research direction for more than one century. After some early pioneering work done by Tobias [3] and Smith et al. [4], many stability prediction methods have been presented, which can be sketchily divided into three classes: frequency domain, time domain, and time simulation. The former two methods are much sought after due to the wide applications and high efficiency. For example, Altintas et al. [5] presented a harmonic balance and infinite determines method based on zero order Fourier transform of cutting force, which is suitable for large radial immersion cases. For low radial immersion cases, more than one Fourier items are necessary to catch the flip bifurcation induced by loss contact between cutter and workpiece [6]. In this case, time discretization methods, such as semi-discretization method (SDM) [7], full-discretization method (FDM) [8], temporal finite element method (TFEM) [9], differential quadrature method (DQM) [10], Chebyshev collocation method (CCM) [11], spectral element method (SEM) [12], and so on, are more adept at handling the discontinuous cutting. These studies have led to graphic charts (stability lobe

diagram, SLD) showing the stability information as a function of cutting depth and spindle speed. However, all these studies assumed that the dynamic characteristics of the system did not change during the whole machining process.

For thin-walled workpiece milling, the dynamic characteristics of cutting process are time varying with the motion of the cutter [13, 14], which is caused by two key factors. One is that the relative space location between cutter and workpiece is time varying. The other is that the material is removed during the machining process. So the stability also changes during the machining process, and the 3D SLD appears, where the third coordinate axis is cutting position. Budak et al. [15] predicted the stability lobes of a cantilevered thin plate milling. Ukar et al. [16] and Bravo et al. [17] presented the frequency domain method to predict the stability with the assumption of both the mass and rigidity reducing continuously during the milling process. Thevenot et al. [18, 19] determined optimal cutting conditions during thin-walled workpiece machining process by three-dimensional stability lobes and conducted analysis on the influence of material removal on the stability. Song et al. [20] proposed a method for predicting simultaneous dynamic stability limit of thin-walled workpiece high-speed milling process using Sherman-Morrison-Woodbury formulas. However, in the above works, only one mode of the structure is considered. Actually, during milling of thin-walled workpiece, with the motion of the cutter, the modal parameters of each mode also change significantly. Seguy et al. [21] studied the stability of thin-wall milling with the first three modes. The results show that all these modes have a significant influence on determining the limited cutting depth. Zhang et al. [22, 23] predicted the stability of flexible part milling with the moving cutting position using finite element method (FEM). However, in most of these analyses, the extraction of the modal parameters is realized by the experimental modal analysis (EMA) and FEM, where the efficiency is very low. For FEM, the workpiece model needs to be updated for each modal analysis step. Meanwhile, it is very time consuming when dealing with a workpiece with various complex boundary conditions, especially for non-classical constraints. So the high-efficiency approach to identify the time-varying dynamic characteristics of workpiece is absent.

Therefore, the primary purpose of this paper is to propose a comprehensive method to investigate the effects of engagement position between cutter and workpiece and multi-modes on the time-varying dynamic characteristics of thin-walled component milling process with arbitrary boundary conditions. The remainder of this paper is summarized as follows: the model of thin-walled part milling with various boundary conditions is presented in Section 2. Then, the modal analysis and time-space discretization method to predict the stability lobes are illustrated in Section 3, and two case studies are performed in Section 4 as well as experimental validation to explain the reliability, efficiency, and accuracy of the method presented. The conclusions are drawn in the last section.

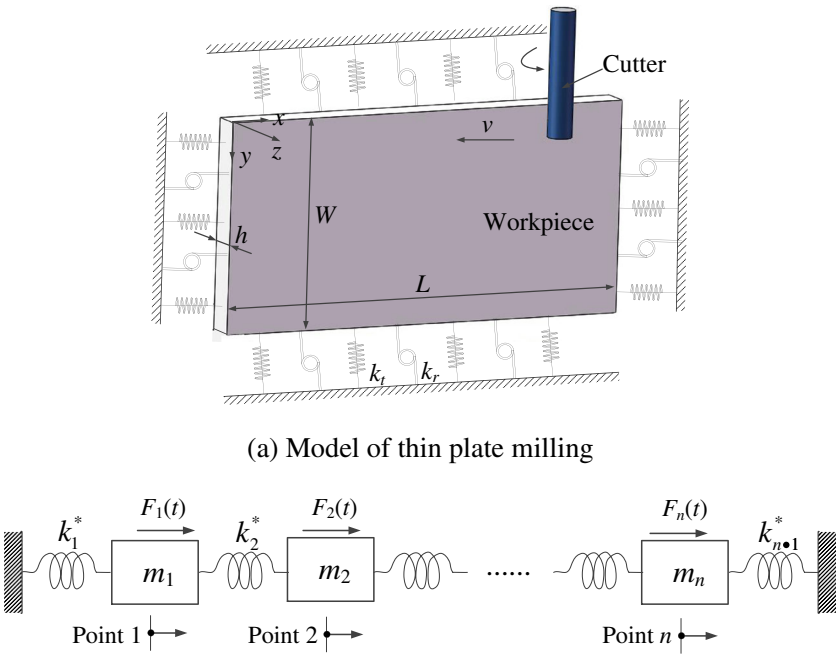

(a) Model of thin plate milling

(b) The n degrees of freedom dynamic model

Fig. 1 Dynamic model of thin-walled component milling

2 Model of thin-walled component milling with various boundary conditions

Due to the high flexibility of thin-walled workpiece in one direction (transverse direction), one degree of freedom model was usually assumed [15]. As described in the previous section, however, the dynamic characteristics are time varying because of the motion of cutter. So in the transverse direction of the workpiece, a continuous system should be modeled, which corresponds to the whole cutting process. In this section, the equation of motion (EOM) of continuous system for thin-walled component milling is proposed based on the thin plate theory and Rayleigh-Ritz solution together with the penalty method.

For the thin-walled component with various boundary conditions, the spring penalty method [24] is employed here to handle the arbitrary constraints. Without loss of generality, a rectangular thin plate with length in L, width in W, and thickness in h is shown in Fig. 1a, where the four edges of the plate are connected with artificial translational and rotational springs to handle the various constraints. Also, Ω is the rotational angle velocity of the cutter. It should be noted that different boundary conditions are expressed as different combinations of stiffness of these springs. For example, as shown in Fig. 1a, if the Edge 1 (x = 0) of the plate is clamped, this constraint is realized by adding some artificial springs with high non-dimensional stiffness to model constraints, where translational springs are used to limit the transverse displacement, w, and torsional springs are applied to limit the rotation, $w_{,x}$, and $w_{,y}$. The additional spring coefficient is named as penalty parameter.

As we know, dynamic characteristics change with respect to the cutting process (cutting position or cutter-workpiece engagement position) for thin-walled component milling. Thus, the modal parameters of thin-walled workpiece milling system are functions of both time and space. That is, at different tool-workpiece engagement positions, the different vibration systems are induced and even subjected to the same milling force. Additionally, considering the workpiece's internal damping and contact damping between the workpiece and fixture, the workpiece model can be regarded as a structural damping system with n degrees of freedom (DOF), as shown in Fig. 1b, where the spring with complex stiffness is used to connect two mass points. Note that the value n really approaches to infinity for the continuous system.

The classical plate theory [25] is used here, and only the bending effect of thin-walled plate is considered. Correspondingly, the strain energy is expressed as

$$V=\frac{D}{2}\iint_A\left[\left(\frac{\partial^2 w}{\partial x^2}\right)^2+\left(\frac{\partial^2 w}{\partial y^2}\right)^2+2\mu\frac{\partial^2 w}{\partial x^2}\frac{\partial^2 w}{\partial y^2}+2(1-\mu)\left(\frac{\partial^2 w}{\partial x\partial y}\right)^2\right]\mathrm{d}x\mathrm{d}y \tag{1}$$

where w is displacement along z direction (transverse direction), μ is the Poisson ratio, and D is the complex flexural rigidity, which is expressed as

$$D=\frac{Eh^3(1+jg)}{12(1-\mu^2)} \tag{2}$$

where E is the elastic module and g is the loss factor of the workpiece-fixture system.

The kinetic energy of the plate can be written as

$$T=\frac{\rho h}{2}\iint_A \dot{w}^2\,\mathrm{d}x\mathrm{d}y \tag{3}$$

where ρ is the density of the plate and the overdot denotes differentiation with respect to time.

The Rayleigh-Ritz method (RRM) [26] is employed to approximately express the transverse displacement. The $N\times N$-terms Rayleigh-Ritz solutions for the problem are of the following form:

$$w(x,y,t)=\sum_{i=1}^{N}\sum_{j=1}^{N}q_{ij}(t)\xi_i(x)\eta_j(y) \tag{4}$$

where q_{ij} is the Ritz coefficient. $\xi_i(x)$ and $\eta_j(y)$ are admissible functions in x and y directions, respectively. To improve the numerical stability and convergent rate, the combinations of polynomial and trigonometric functions are adopted to be as the admissible functions [27], which are expressed as

$$\begin{aligned} x\text{-direction}: \quad \xi_i(x)&=\begin{cases}\left(\frac{x}{L}\right)^{i-1}, & i=1,2,3\\ \cos\frac{(i-3)\pi x}{L} & i=4,5,\ldots,N\end{cases}\\ y\text{-direction}: \quad \eta_j(y)&=\begin{cases}\left(\frac{y}{W}\right)^{j-1} & j=1,2,3\\ \cos\frac{(j-3)\pi y}{W} & j=4,5,\ldots,N\end{cases}\end{aligned} \tag{5}$$

It is worth noting that the admissible functions adopted here just satisfy a totally unconstrained boundary condition, which is associated with the penalty method [24]. Since the artificial translational and rotational springs are introduced

into the system to restrict the plate's motion, the additional strain energy, V_r, arousing from the deformation of these constraining springs, should be considered and given by

$$V_r = \frac{1}{2}\left(\int_0^W k_{1,\mathrm{t}}\cdot w^2\big|_{x=0}\mathrm{d}y + \int_0^W k_{1,r}\cdot w_{,x}^2\Big|_{x=0}\mathrm{d}y + \int_0^L k_{2,\mathrm{t}}\cdot w^2\big|_{y=0}\mathrm{d}x + \int_0^L k_{2,r}\cdot w_{,x}^2\Big|_{y=0}\mathrm{d}x\right) + \frac{1}{2}\left(\int_0^W k_{3,\mathrm{t}}\cdot w^2\big|_{x=L}\mathrm{d}y + \int_0^W k_{3,r}\cdot w_{,y}^2\Big|_{x=L}\mathrm{d}y + \int_0^L k_{4,\mathrm{t}}\cdot w^2\big|_{y=W}\mathrm{d}x + \int_0^L k_{4,r}\cdot w_{,y}^2\Big|_{y=W}\mathrm{d}x\right) \tag{6}$$

where $k_{,\mathrm{t}}$ and $k_{,\mathrm{r}}$ are the stiffness coefficients of the translational and rotational springs, respectively, and determined by the boundary conditions. For the clamped constraint, both the values of $k_{,\mathrm{t}}$ and $k_{,\mathrm{r}}$ are 1×10^9, and both are zero for free boundary condition in this paper.

Since the main aim is to extract the modal parameters, the external work done by the milling force is neglected. Therefore, the Lagrange of this system without load is $L = T - V - V_r$, and the equation of motion (EOM) of the continuous system obtained by Lagrange's equation is shown as

$$\mathbf{S}\{\ddot{q}\} + \mathbf{U}\{q\} = \{0\} \tag{7}$$

where the double-overdot denotes second-order differentiation with respect to time, $\{\mathbf{0}\}$ is column vector of $N^2 \times 1$, $\{q\} = \{q_{11}\ q_{12}\ \ldots\ q_{NN}\}^T$, and

$$S_{uv} = \rho h \int_0^L \int_0^W \xi_i \xi_j \eta_m \eta_n \mathrm{d}x\mathrm{d}y \tag{8}$$

$$\begin{aligned} U_{uv} = D\iint_A & \left[\begin{array}{l} \xi_{i,xx}\xi_{j,xx}\eta_m\eta_n + \xi_i\xi_j\eta_{m,yy}\eta_{n,yy} + \mu\left(\xi_{i,xx}\xi_j\eta_m\eta_{n,yy} + \xi_i\xi_{j,xx}\eta_{m,yy}\eta_n\right) \\ +2(1-\mu)\xi_{i,x}\xi_{j,x}\varphi_{m,y}\varphi_{n,y} \end{array}\right]\mathrm{d}x\mathrm{d}y \\ & + \xi_i(0)\xi_j(0)\int_0^W k_{1,t}\eta_m\eta_n\mathrm{d}y + \xi_{i,x}(0)\xi_{j,x}(0)\int_0^W k_{1,r}\eta_m\eta_n\mathrm{d}y \\ & + \eta_m(0)\eta_n(0)\int_0^L k_{2,t}\xi_i\xi_j\mathrm{d}x + \eta_{m,y}(0)\eta_{n,y}(0)\int_0^L k_{2,r}\xi_i\xi_j\mathrm{d}x \\ & + \xi_i(1)\xi_j(1)\int_0^W k_{3,t}\eta_m\eta_n\mathrm{d}y + \xi_{i,x}(1)\xi_{j,x}(1)\int_0^W k_{3,r}\eta_m\eta_n\mathrm{d}y \\ & + \eta_m(1)\eta_n(1)\int_0^L k_{4,t}\xi_i\xi_j\mathrm{d}x + \eta_{m,y}(1)\eta_{n,y}(1)\int_0^L k_{4,r}\xi_i\xi_j\mathrm{d}x \end{aligned} \tag{9}$$

In Eqs. (8) and (9), $u = m + (i-1)\times N$ and $v = n + (j-1)\times N$, here i, j, m, and $n = 1, 2, \ldots, N$. The $(\cdot)_{,x}$ represents the first-order differentiation with respect to x, which is similar with $(\cdot)_{,xx}$, $(\cdot)_{,y}$, and $(\cdot)_{,yy}$.

3 Time-space discretization method

3.1 Natural frequency and loss factor

Equation (7) describes the plate's free vibration and can be used to extract the natural frequencies and loss factors. Assuming $\{q(t)\}$ in the form of $\{\bar{q}\}\, e^{i\lambda t}$, Eq. (7) can be rewritten as

$$\left(\mathbf{U} - \lambda^2\mathbf{S}\right)\{\bar{q}\} = \{0\} \tag{10}$$

Since the stiffness matrix $\mathbf{U}$ is a complex matrix, the generalized eigenvalue, λ^2, is also a complex number. As a result, the derived complex eigenvalue problem, Eq. (10), gives the r-order natural frequency ω_r and loss factor g_r as follows:

$$\omega_r = \sqrt{\mathrm{Re}\left[\lambda_r^2\right]} \text{ and } g_r = \frac{\mathrm{Im}\left[\lambda_r^2\right]}{\mathrm{Re}\left[\lambda_r^2\right]} \tag{11}$$

where Re[·] and Im[·] mean real and imaginary parts, respectively. For small loss factor, it has the following relationship with damping ratio [28]:

$$g_r = 2\zeta_r \tag{12}$$

Having determined the natural frequencies and loss factors, the FRF of the plate is now of primary interest for extracting

the modal parameters of the system. Assuming a unit harmonic point load applied at point (x_{in}, y_{in}), the FRF with response to point (x_{re}, y_{re}) can be calculated as

$$H(\omega) = \{W(x_{re}, y_{re})\}^T \left(-\omega^2 \mathbf{S} + \mathbf{U}\right)^{-1} \{W(x_{\text{in}}, y_{\text{in}})\} \tag{13}$$

where $\{W(x,y)\} = \{\xi_1(x)\eta_1(y)\ \xi_2(x)\eta_2(y)\ \ldots\ \xi_N(x)\eta_N(y)\}^T$, and **S** and **U** are calculated by Eqs. (8) and (9), respectively.

3.2 Modal parameter identification

Up to now, the natural frequencies, loss factors, FRFs, and modal shapes of thin plate have been calculated using the continuous system model in the previous section. For the stability prediction of thin-walled component milling, the modal parameters corresponding to each engagement position of cutter and workpiece are necessary. Thus, in this section, the continuous system is firstly regarded as *n*-DOFs discrete model based on spatial discrete operation, and then the modal parameters of the discrete model are identified and extracted using modal superposition principle [29].

Before extracting modal parameters, a structural damping system with *n*-DOFs as shown in Fig. 1b is firstly studied. The equation of motion of the spring-mass system is

$$\mathbf{M}\{\ddot{x}\} + \mathbf{K}^*\{x\} = \{F(t)\} \tag{14}$$

where $\{F(t)\} = \{F_1(t)\ F_2(t)\ \ldots\ F_n(t)\}$, $\{x\} = \{x_1\ x_2\ \ldots\ x_n\}$, and

$$\mathbf{M} = \begin{bmatrix} m_1 & 0 & 0 & \cdots & 0 & 0 \\ 0 & m_2 & 0 & \cdots & 0 & 0 \\ 0 & 0 & m_3 & \cdots & 0 & 0 \\ \vdots & \vdots & \vdots & \ddots & \vdots & \vdots \\ 0 & 0 & 0 & \cdots & m_{n-1} & 0 \\ 0 & 0 & 0 & \cdots & 0 & m_n \end{bmatrix} \tag{15}$$

$$\mathbf{K}^* = \begin{bmatrix} k_1^* + k_2^* & -k_2^* & 0 & \cdots & 0 & 0 \\ -k_2^* & k_2^* + k_3^* & -k_3^* & \cdots & 0 & 0 \\ 0 & -k_3^* & k_3^* + k_4^* & \cdots & 0 & 0 \\ \vdots & \vdots & \vdots & \ddots & \vdots & \vdots \\ 0 & 0 & 0 & \cdots & k_{n-1}^* + k_n^* & -k_n^* \\ 0 & 0 & 0 & \cdots & -k_n^* & k_n^* + k_{n+1}^* \end{bmatrix} \tag{16}$$

To decouple Eq. (14), the generalized eigenvectors, ϕ_1, ϕ_2, …, ϕ_n, are used, and the conversions are shown as

$$\boldsymbol{\Phi}^T \mathbf{M} \boldsymbol{\Phi} = \overline{\mathbf{M}}_{dia} \quad \text{and} \quad \Phi^T \mathbf{K}^* \Phi = \overline{\mathbf{K}}^*_{dia} \tag{17}$$

where both $\overline{\mathbf{K}}^*_{dia}$ and $\overline{\mathbf{M}}_{dia}$ are diagonal matrices, and $\boldsymbol{\Phi} = [\phi_1\ \phi_2\ \ldots\ \phi_n]$. The generalized eigenvalues are calculated by

$$\lambda_r^2 = \frac{\overline{k}_r^*}{\overline{m}_r} = (1 + jg_r)\frac{\overline{k}_r}{\overline{m}_r} = (1 + jg_r)\omega_r^2 \tag{18}$$

where $\overline{m}_r$, $\overline{k}_r$, and g_r are the *r*-order modal mass, mass stiffness, and loss factor, respectively.

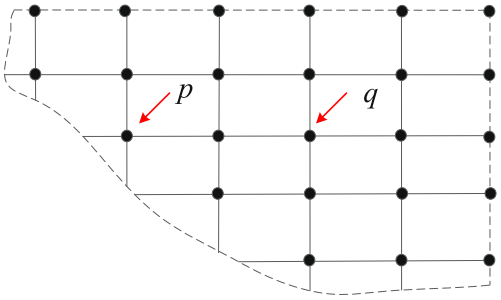

Fig. 2 The discrete plate model with finite degrees of freedom

Conducting Fourier transform on Eq. (14), the frequency response function (FRF) is given by

$$\mathbf{H}(\omega) = \frac{1}{\mathbf{K}^* - \omega^2 \mathbf{M}} = \frac{1}{(\mathbf{I} + j\mathbf{G})\mathbf{K} - \omega^2 \mathbf{M}} \tag{19}$$

where **G** is matrix of loss factor, and both **G** and **K** are real matrices. Based on Eq. (17), the specific expression of FRF is written as

$$\mathbf{H}(\omega) = \sum_{r=1}^{n} \frac{\phi_r^T \phi_r}{\overline{m}_r\left[(1 + jg_r)\omega_r^2 - \omega^2\right]} \tag{20}$$

Therefore, $\mathbf{H}(\omega)$ is a symmetric matrix, and $H_{lp}(\omega)$ represents the FRF of exciting on point *p* and response on point *l*, and is given by

$$H_{lp}(\omega) = \sum_{r=1}^{n} \frac{\varphi_{lr}\varphi_{pr}}{\overline{m}_r\left[(1 + jg_r)\omega_r^2 - \omega^2\right]} \tag{21}$$

where $\{\varphi_1\ \varphi_2\ \ldots\ \varphi_n\}_r = \phi_r$. According to the rational fraction method, $H_{lp}(\omega)$ can be transformed as

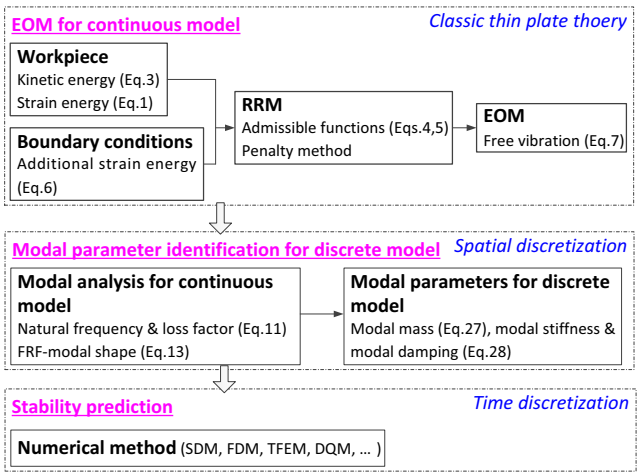

Fig. 3 Time-space discretization method for stability prediction

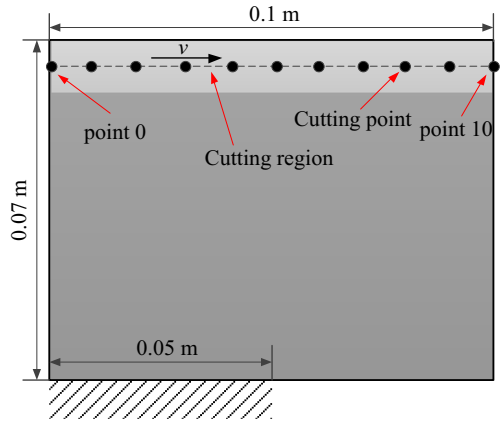

Fig. 4 Model of the half-clamped plate

$$H_{lp}(\omega) = \sum_{r=1}^{n} \left(\frac{A_{lpr}}{\alpha\omega_r - \omega} + \frac{-A_{lpr}}{-\alpha\omega_r - \omega} \right) \tag{22}$$

where A_{lpr} is residue of the r-order modal and given by

$$A_{lpr} = \frac{\varphi_{pr}\varphi_{lr}}{2\alpha\omega_r \bar{m}_r} \quad \text{with } \alpha = \sqrt{1 + jg_r} \tag{23}$$

For a given milling system, the natural frequency and loss factor or damping ratio are determined using Eq. (11). However, the modal mass and modal stiffness are related to the modal shape (see Eq. (17)). As shown in Fig. 2, a continuous plate is divided into finite points.

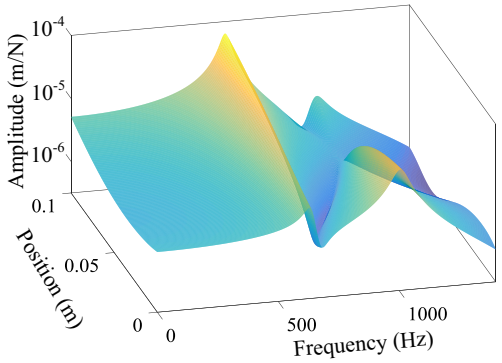

Fig. 6 Three-dimensional FRF of the half-clamped plate

When the cutting force is applied on point p, the transverse vibration of this point is of primary interest, which directly relates to the machined surface quality. Assuming r-order modal dominates the plate's vibration, the equation of motion of the cutting point p is

$$\frac{\bar{m}_r}{\varphi_{pr}^2}\ddot{x}_p + \frac{\bar{c}_r}{\varphi_{pr}^2}\dot{x}_p + \frac{\bar{k}_r}{\varphi_{pr}^2}x_p = F_t \tag{24}$$

where φ_{pr} represents the p-term in eigenvector of r-order modal and F_t is the cutting force. When the cutter moves to point q, the φ_{pr} also changes as φ_{qr}. Therefore, the modal parameters are different for different cutting location points during the milling process. From Eq. (24), it also can be seen that the

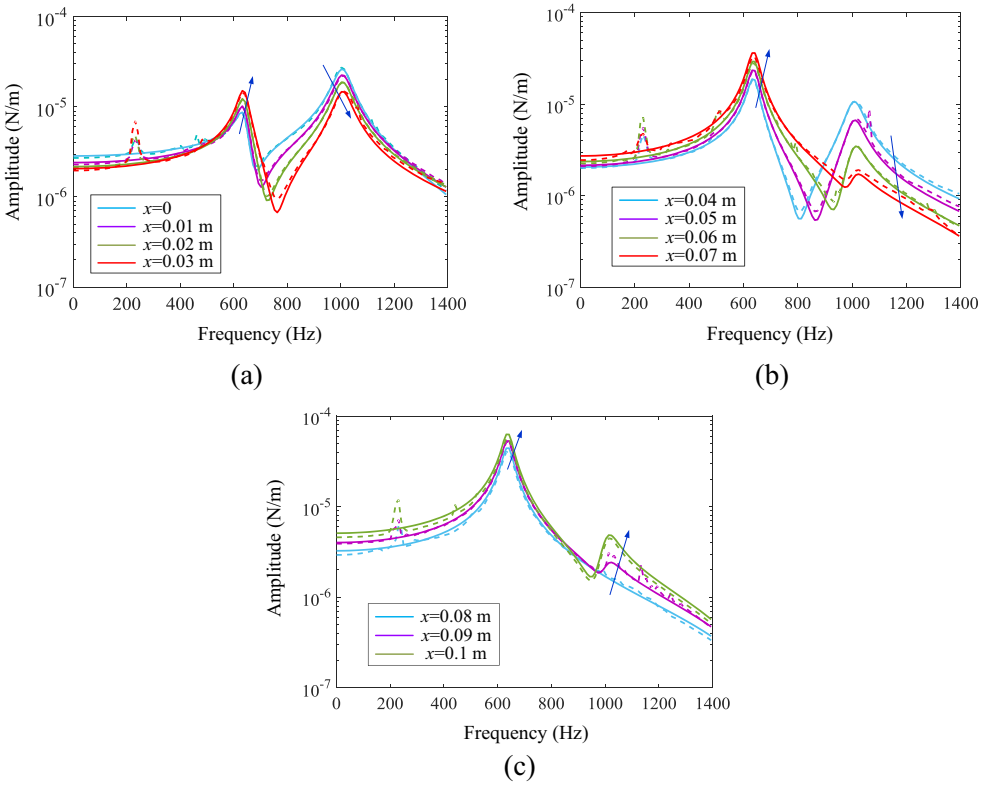

Fig. 5 FRFs of the selected points. *Dashed line*: experimental FRFs; *solid line*: theoretical FRFs

Table 1 The modal parameters of the first two modes

Position number	First order			Second order		
	Modal mass (kg)	Modal stiffness ($\times 10^6$ N/m)	Modal damping (N·s/m)	Modal mass (kg)	Modal stiffness ($\times 10^6$ N/m)	Modal damping (N·s/m)
0	0.1340	2.15	35.27	0.0147	0.59	6.04
1	0.1032	1.66	27.16	0.0170	0.68	7.00
2	0.0810	1.30	21.29	0.0204	0.82	8.40
3	0.0639	1.03	16.78	0.0260	1.04	10.70
4	0.0504	0.81	13.25	0.0363	1.46	14.94
5	0.0399	0.64	10.48	0.0587	2.35	24.15
6	0.0318	0.51	8.35	0.1233	4.94	50.74
7	0.0250	0.41	6.73	0.4800	19.37	199.23
8	0.0210	0.34	5.51	–	–	–
9	0.0175	0.28	4.59	0.3831	15.35	157.81
10	0.0148	0.24	3.89	0.0990	3.97	40.77

ratio of the modal parameters at different cutting location points equals to the quadratic of the inverse ratio of their modal shapes at a specific modal, namely

$$\frac{\bar{m}_{pr}}{\bar{m}_{qr}} = \frac{\varphi_{qr}^2}{\varphi_{pr}^2} \tag{25}$$

Assuming the system resonates at r-order modal, namely $\omega = \omega_r$, if the modal density is not high in this resonant region, other modals' effects can be neglected, and Eq. (22) can be written as

$$H_{lp}(\omega) = \frac{A_{lpr}}{\alpha\omega_r - \omega} + \frac{-A_{lpr}}{-\alpha\omega_r - \omega} \tag{26}$$

Here, the residue, A_{lpr}, in Eq. (26), can be extracted from the determined FRF.

For simplicity, the modal shape of a specific modal on the cutting location points is usually taken as one. In this condition, the modal mass on this point is given by

$$\bar{m}_{pr} = \frac{1}{|2A_{ppr}\alpha|} \tag{27}$$

The corresponding modal stiffness and modal damping are given by

$$\bar{k}_{pr} = \bar{m}_{pr}\omega_r^2 \quad \text{and} \quad \bar{c}_{pr} = 2\bar{m}_{pr}\zeta_r\omega_r \tag{28}$$

3.3 Stability prediction procedure

For thin-walled workpiece, the transverse vibration is more serious than the plane vibration. Therefore, n-DOFs milling model in transverse direction is adopted (Fig. 1b). The stability prediction procedure for TSDM can be illustrated in Fig. 3 and summarized as follows:

Step 1. The equation of motion (EOM) of continuous system is modeled based on the *classical thin plate theory*,

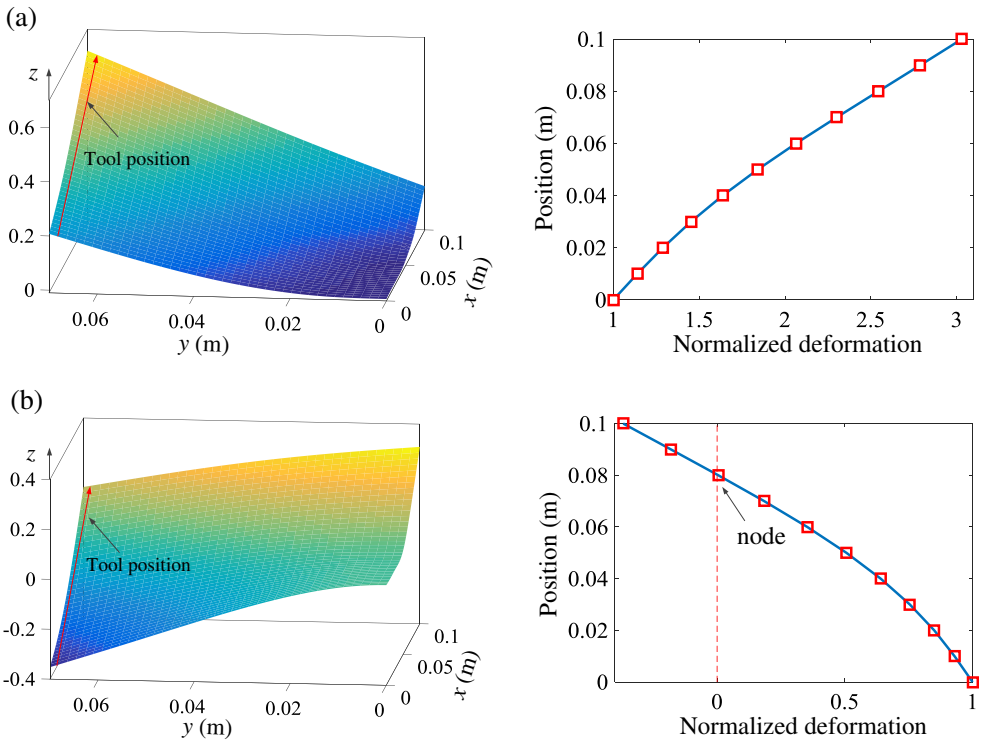

Fig. 7 The first two modal shapes (*left diagrams*) and normalized deformations (*right diagrams*) along the tool path. **a** First mode; **b** second mode

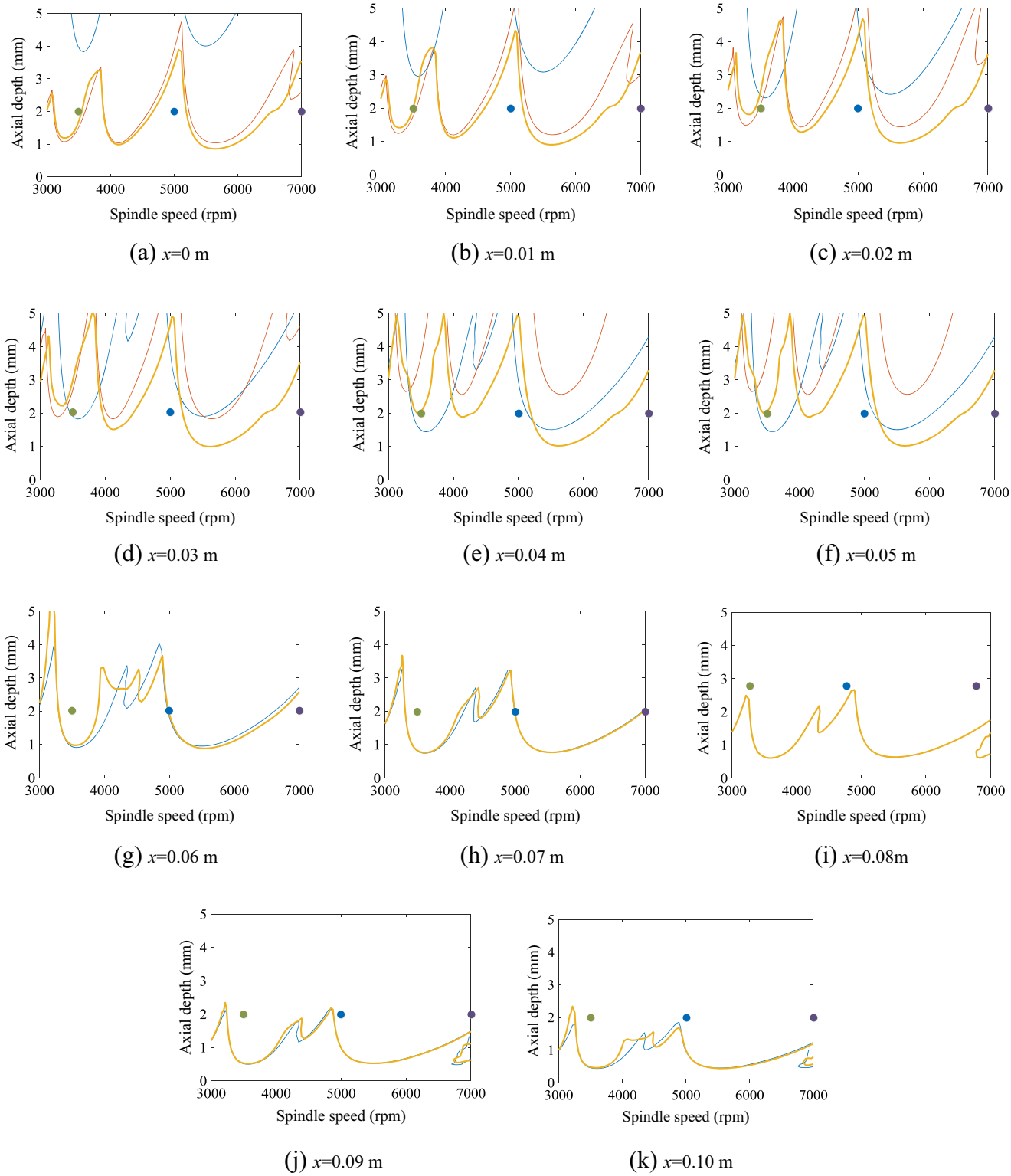

Fig. 8 Dynamic SLDs for the milling process with different modes. *Blue thin line*: first order mode; *red thin line*: second order mode; *orange bold line*: the first two order modes; *green dot*: n = 3500 rpm; *blue dot*: n = 5000 rpm; *black* dot: n = 7000 rpm

Rayleigh-Ritz method together with penalty method and Lagrange equation, including kinematic energy (Eq. (3)), strain energy (Eq. (1)), and additional strain energy (Eq. (6)).

Step 2. Modal analysis, including natural frequency and loss factor (Eq. (11)), frequency response function, and modal shape (Eq. (13)), is performed for continuous model. Then the continuous system is assumed as *n*-

DOFs discrete model based on *spatial discrete operation*. Also, the modal parameters (modal mass, modal stiffness, and modal damping, Eqs. (27) and (28)) corresponding to each engagement position of cutter and workpiece for discrete model are identified using mode superposition principle.

Step 3. Stability prediction is carried on using *time domain methods* (e.g., SDM [7], FDM [8], TFEM [9], DQM [10], and so on) existed in articles based on the modal parameters identified in the previous step, which are time varying and are dependent of relative space position between cutter and workpiece being machined. It is should be emphasized that the traditional cutting model [31] of the milling process is used here.

4 Results analysis

In this section, the experimental and numerical analysis is conducted to validate the proposed method, and the stability of the flexible workpiece milling with different boundary conditions is investigated. It should be emphasized that the convergence and flexibility of the method presented to deal with the dynamic response of thin plate with arbitrary boundary conditions have been verified in Ref. [30]. The size of the thin-walled plate used here, otherwise specified, is 0.1 × 0.07 × 0.005 m. The material of the part is aluminum alloy, with a density of 2740 kg/m^3, Young's modulus of 70 GPa, and Poisson's ratio of 0.33. A milling cutter with four teeth and 12 mm diameter is used in the down-milling process. The lower radial immersion ratio, 0.4/12 (≈3.33 %), is selected here in order to ignore the effect of material removal, which have been illustrated using several numerical methods in many publications, such as finite element method [13, 14, 19] and structural dynamic modification method [20]. It should be noted that the method presented here can also be used to consider this effect, which will be investigated clearly in another future article. Also, the tangential and normal cutting force coefficients are $K_t = 5.4 \times 10^8$ N/m^2 and $K_n = 1.8 \times 10^8$ N/m^2, respectively [13]. The following two case studies are presented.

4.1 Case study I: a half-clamped thin plate milling and experimental validation

Figure 4 shows the model of the workpiece. Without loss of generality, in this case, only half of one edge is clamped to create a casual boundary condition. In order to describe the dynamic characteristics of the plate, 11 evenly distributed points are selected along the cutter path. It should be mentioned that before conducting the modal analysis, the impact test should be firstly performed to obtain the loss factor of the plate. Based on Eq. (12), the structural loss factor is assumed as the average value of each concerned modal loss factor. Since the loss factor remains unchanged with the variation of the tool position, only one impacted point is needed. It should be noted that all stiffness coefficients ($k_{,r}$ and $k_{,t}$ in Eq. (6)) for three free edges are zero, and the coefficients of half-clamped edge are the larger value (such as 1×10^9) from L = 0–0.05 m and zero from L = 0.05–0.1 m, respectively.

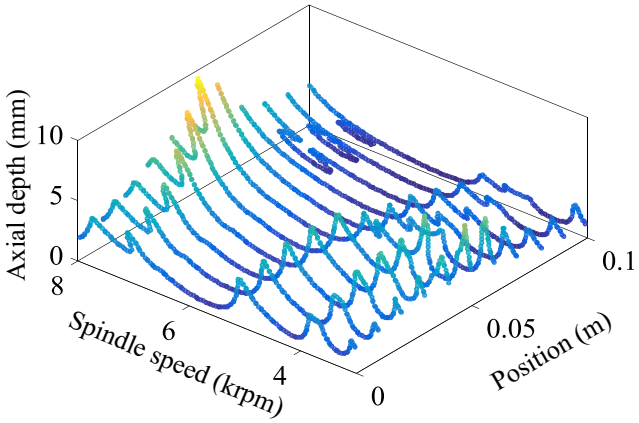

Fig. 9 The three-dimensional SLD of the half-clamped plate milling

Figure 5 illustrates the theoretical and experimental FRFs of the 11 selected points. It can be seen that the good agreement between these two kinds of results verifies the accuracy of the proposed modal analysis method. As predicted, the natural frequency (location of the peaks) and damping ratio (slope of the peaks) stand at a stable value in these 11 points. The first and second natural frequencies are 642 and 1023 Hz, respectively, and the corresponding damping ratios are both 0.034. However, the magnitude of dominant modal response changes a lot, which determinates the modal parameters of each position. It is noted that in the range of 0–0.03 m (Fig. 5a), the second mode dominates the response, while for

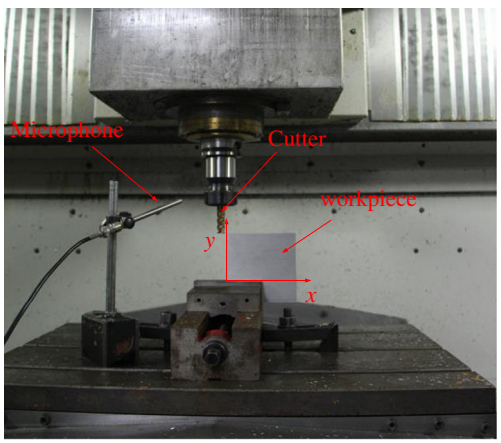

Fig. 10 Experimental setup

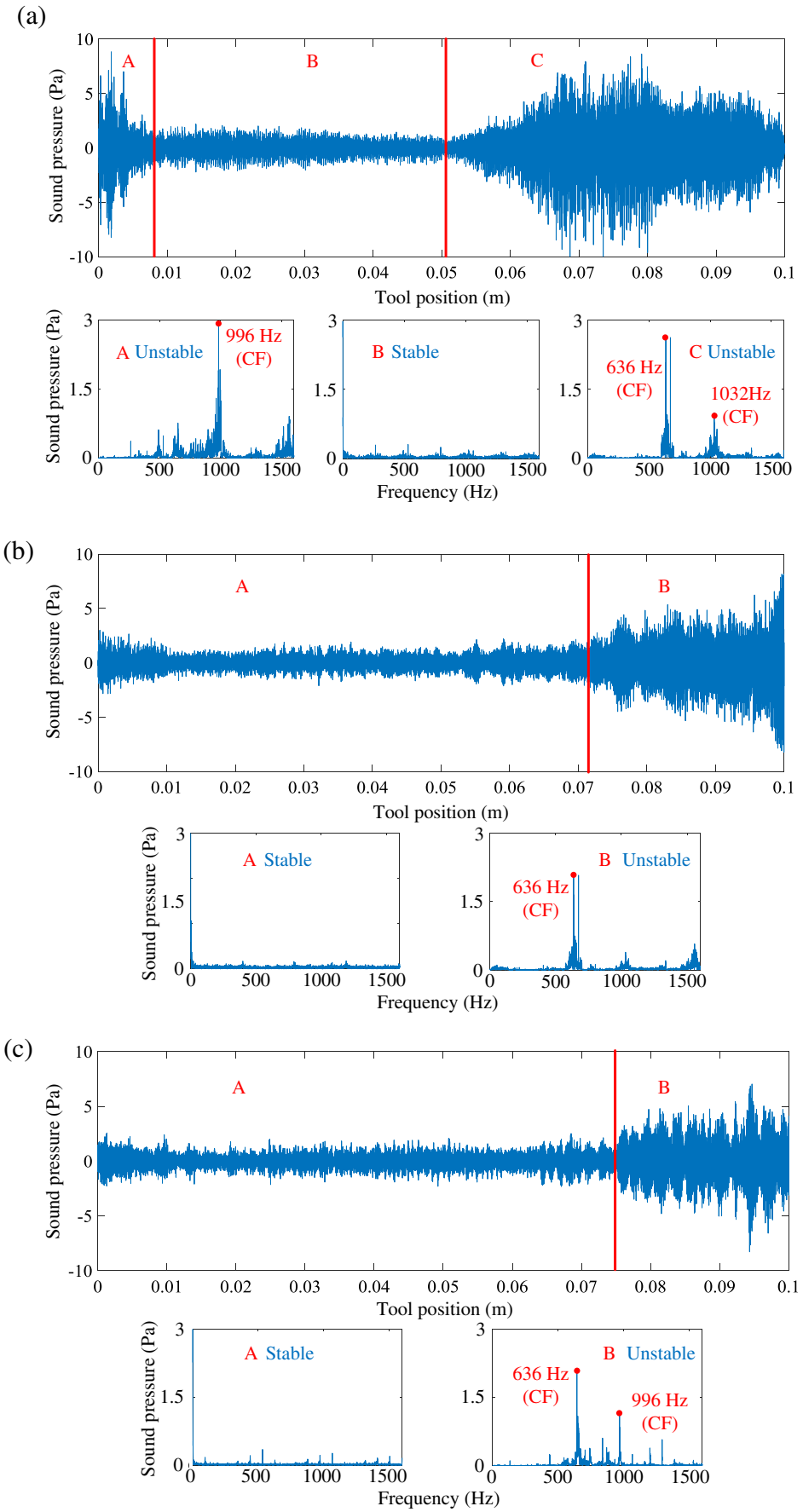

Fig. 11 The time domain and frequency domain sound signals measured. **a** n = 3500 rpm; **b** n = 5000 rpm; **c** n = 7000 rpm

Table 2 Comparisons of ranges of stable domain and chatter domain between simulation and experiment

Spindle speed (rpm)	Stable domain of simulation (m)	Stable domain of experiment (m)	Chatter domain of simulation (m)	Chatter domain of experiment (m)
3500	0–0.01, 0.05–0.10	0–0.008, 0.05–0.10	0.01–0.05	0.008–0.051
5000	0–0.07	0–0.072	0.07–0.10	0.072–0.10
7000	0–0.07	0–0.074	0.07–0.10	0.074–0.10

0.03–0.10 m, the pattern is in the opposite. In addition, the magnitude of the first mode keeps an increasing trend along the tool path, while that of the second mode firstly decreases to null in $x = 0.08$ m (Fig. 5c), and then has a small rise. Figure 6 gives the three-dimensional FRF of the workpiece and clearly shows the trend indicated in Fig. 5.

Based on the theoretical analysis in Section 3.2, the modal parameters of the workpiece can be extracted from the obtained FRF. Table 1 gives the first two modal parameters of the half-clamped plate. It is easy to find that with the motion of the cutter, the first-order modal parameters decrease continuously to about 0.11 times of those of position 0. By contrast, the modal parameters of second mode firstly increases sharply from position 0 ($x = 0$ m) to position 7 ($x = 0.07$ m) (increasing by 11 times) and disappears in position 8 ($x = 0.08$ m). After that, a reverse trend occurs from position 9 ($x = 0.09$ m) to position 10 ($x = 0.10$ m). The opposite tendency of the FRF (or modal parameters) can be explained by Eq. (25). As shown in Fig. 7, the first modal shape is a bend deformation. However, due to the asymmetric constraint, the deformation of the tool path increases by three times from position $x = 0$ to $x = 0.10$ m. Based on Eq. (25), the modal parameters of the same order has an inverse quadratic relationship with the deformation. Therefore, the increasing deformation of the tool path results in the continuous decrease of the modal parameters. The reason can also be used to explain the tendency of the second-order modal parameters. However, it should be mentioned that the torsional deformation of the plate brings in a node on position $x = 0.08$ m. Therefore, the modal parameters on position $x = 0.08$ m can be considered as an infinite value.

Figure 8 illustrates the stability lobe diagrams (SLDs) of the 11 selected points using the TSDM presented in the above section. As shown in Fig. 8a–c, the limited axial depth is mainly determinated by the second mode. However, when the cutter moves to the right side of the plate, the limited value are gradually identical with that calculated by the first modal parameters. This may be because the second modal plays a more important role in the response of the left part of the plate, while for position $x = 0.02$–0.10 mm, the first mode determinates the response of the plate (see Fig. 6). Based on the theoretical SLD, the predicted stable area of the green dot (axial depth is 2 mm, spindle speed is 3500 rpm) is 0.01–0.05 m, while that of the blue dot (axial depth of cut is 2 mm, spindle speed is 5000 rpm) and black dot (axial depth of cut is 2 mm, spindle speed is 7000 rpm) are both 0–0.07 m. A more clear description of the SLD is shown in Fig. 9.

To verify the correctness of the predicted stability, the milling experiment is carried out on a high-speed machining center VMC0540d with a maximum spindle speed of 30,000 rpm. A GRAS 40PP microphone with sensitivity of 50 mV/Pa is used to measure the sound pressure. The milling experimental setup is shown in Fig. 10. The material of the workpiece is aluminum alloy 7075, whose geometric parameters are described previously, and the material of tool is cemented carbide. The diameter of the cutter is 12 mm, and the feed rate is 600 mm/min. To validate the accuracy of the calculated SLD, three sets of cutting parameters are specially selected, where the axial depth of cut is 2 mm and the spindle speeds are 3500, 5000, and 7000 rpm, respectively.

Figure 11 shows the measured time domain and frequency domain signals of the sound pressure. CF indicates chatter frequency. When the spindle speed is 3500 rpm, based on the magnitude of the pressure, the sound signal along the tool position is divided into three different regions, namely A, B, and C (see Fig. 11a). These three regions range from 0 to 0.008 m, 0.008–0.051 m, and 0.051–0.10 m, respectively. To detect the stability of these durations, their frequency domain analyses are conducted separately. For duration A, the

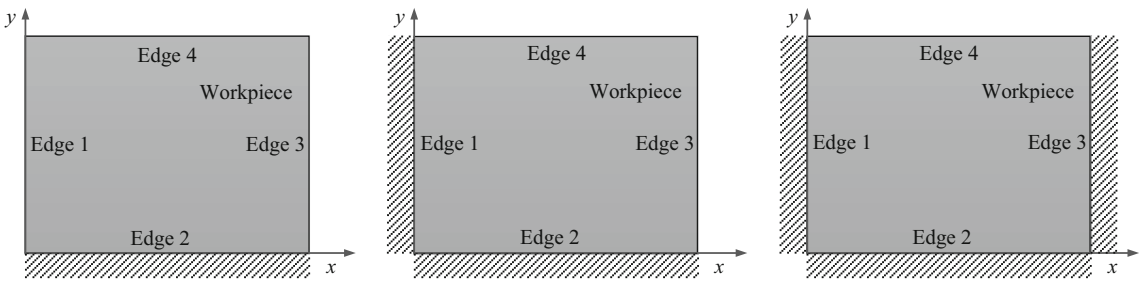

(a) FCFF (b) CCFF (c) CCCF

Fig. 12 The plates with different boundary conditions

pressure concentrates on 996 Hz, which is near the second natural frequency, 1023 Hz, of the plate. This is because the SLD of the left part of the half-clamped plate is mainly determined by the second modal parameters. By contrast, for duration C, when the cutter moves to the right side of the plate, the pressure mainly focuses on 636 Hz (near the first natural frequency, 624 Hz). There is also a small part that concentrates on 1032 Hz. This may account for the dominance of the first mode in determining the stability limit of the right area of the workpiece. A similar phenomenon can also be observed in Fig. 11b and c. Therefore, in the first cutting condition (spindle speed is 3500 rpm and axial depth of cut is 2 mm), the stable region is 0.008–0.051 m, and the unstable region is 0–0.008 m and 0.051–0.1 mm. For the second and third cutting conditions, the correspondingly stable regions are 0–0.072 m and 0–0.074 m, respectively, while the unstable regions are 0.072–0.10 m and 0.074–0.10 m.

In the comparison of the ranges of stable domain and chatter domain between simulation and experiment shown in Table 2, two results are in good agreement. Thus, the correctness of the proposed method can be verified.

4.2 Case study II: thin plate milling with various boundary conditions

After the validation of the proposed method, in this case, a thin-walled plate with three different boundary conditions are studied to explain the capacity of presented method for handling various boundary conditions. The cases where the method is applied to more non-classical boundary conditions can be found in Ref. [30]. For the sake of brevity, a counterclockwise notation starting from $x = 0$ is utilized to identify the boundary conditions of the plate. For example, the symbol "CSFC" represents a plate with the clamped edge (C) at $x = 0$, simply supported (S) at $y = W$, free (F) at $x = L$, and clamped (C) at $y = 0$. As shown in Fig. 12, the plate with FCFF, CCFF, and CCCF are modeled. Both stiffness coefficients ($k_{,r}$ and $k_{,t}$ in Eq. (6)) of the free edge are zero, and the coefficients of the clamped edge are 1×10^9.

Figure 13 shows the three-dimensional FRFs (Fig. 13a) and the first two order mode shapes (Fig. 13b, c) of these three

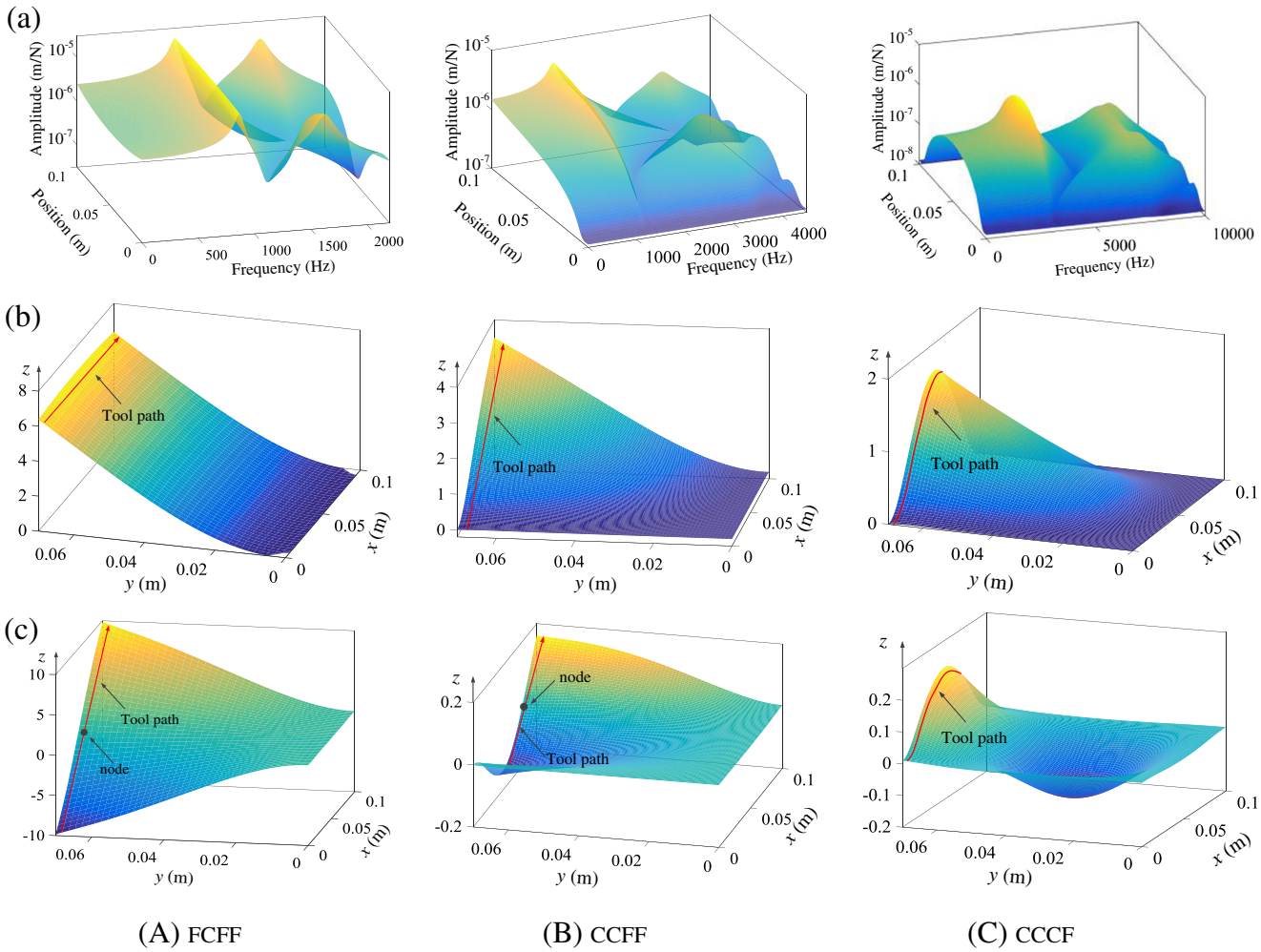

Fig. 13 3D-FRFs (**a**) and the first two modal shapes (**b**, **c**) of the plates with different boundary conditions

different workpieces. As shown in Fig. 13a, due to the symmetry of the constraint, the FRF is also symmetric about the line $x = 0.05$ m. Since the deformation of the first mode shape along the tool path remains unchanged, the first order FRF is also invariable along the position. However, due to the torsional deformation of the second mode, there is a node in the middle area of the tool path and the FRF of this node also changes according to the modal shape. The relationship between the FRFs and the mode shapes can also be found in Fig. 13b and c. However, it should be mentioned that with more edges clamped, the amplitude of the FRF is reduced while the natural frequency improves a lot.

Figure 14 gives the three-dimensional SLDs of these three plates considering only the first order mode (single mode) and the first two modes (multi-modes). For the FCFF plate, it is clear that the single mode SLD is almost the same as the multi-modes SLD in these three boundary conditions, which means the SLD is mainly determined by the first mode. However, there are also some regions where the limited axial depth is mildly influenced by the second mode. For example, the multi-modes' limited axial depth is smaller than that of single mode at the two ends of the tool path. This is because the FRFs of these two positions have a similar magnitude, which means both the first mode and second mode play a similar importance in determining the SLD. However, when the cutter moves to the central position, due to the existence of a node of the second mode, the influence of the second mode is near nonexistent. A similar phenomenon can also be found in the

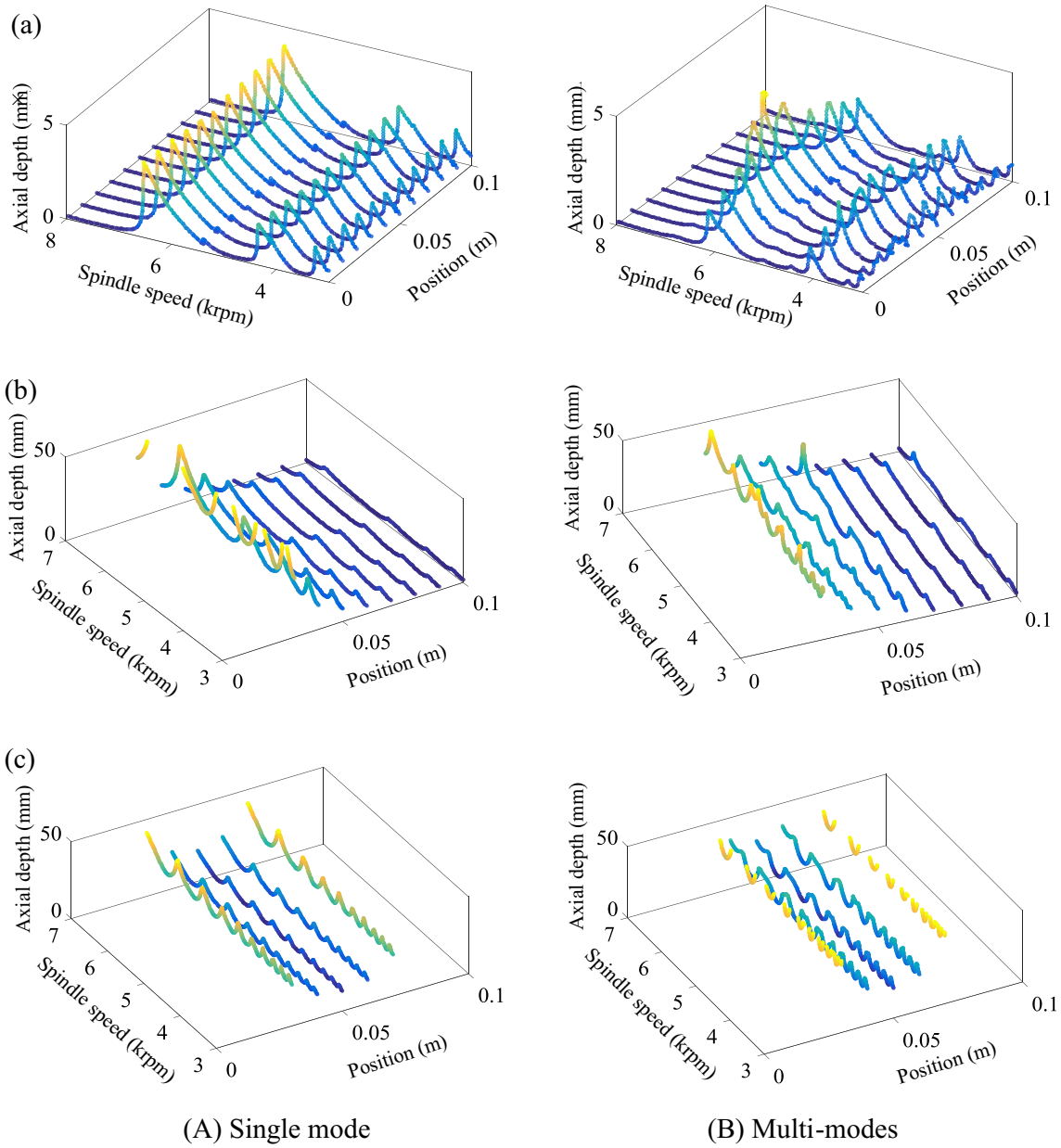

Fig. 14 The three-dimensional SLDs of the three different plates along the tool path. **a** FCFF; **b** CCFF; **c** CCCF

middle region of the CCCF plate. However, for the CCFF plate, due to its asymmetric constraint, the first modal shape varies a lot along the tool path, which causes a great change in the FRF of the first mode. Correspondingly, the second mode mostly influences the limited axial depth in the left part of the tool path. A more clear difference can be found in the case of the half-clamped plate (Fig. 8). Therefore, for the plate with symmetric boundary condition, the first-order modal parameters can be used to predict the stability, while the accuracy for asymmetric plate is greatly affected.

5 Conclusions

In thin-walled workpiece milling process, the dynamic characteristics of the cutting system is time varying, which is caused by two key factors. One is that the relative space location between cutter and workpiece is time varying. The other is that the material is removed during the machining process. Focusing on the time-varying space position between cutter and workpiece, in this paper, a comprehensive time-space discretization method (STDM) is proposed to investigate this effect on the time-varying dynamic characteristics of thin-walled component milling process, as well as multi-modes stability prediction. The experimental results verify the accuracy of the method. It is also found that with the motion of the cutter, the first and second modes show different influence on determining the stability of the workpiece milling. The additional advantage of the STDM presented here is that it can easily handle various boundary conditions of the component, which is particularly useful in practical applications, such as monolithic component milling and blade milling. Additionally, the STDM can also provide an introduction to develop a software for identifying the time-varying modal parameters and predicting stability lobes, which is more effective than FEM.

Acknowledgments This work was supported by grants from Tai Shan Scholar Foundation (no. TS20130922). The authors are grateful to the financial support from the National Natural Science Foundation of China (no. 51575319), the Young Scholars Program of Shandong University (no. 2015WLJH31), and Major National Science and Technology Project (no. 2014ZX04012-014).

References

1. Yi W, Jiang ZL, Shao WX, Han XC, Liu WP (2015) Error compensation of thin plate-shape part with prebending method in face milling. Chin J Mech Eng 28:88–95
2. Song QH, Ju GG, Liu ZQ, Ai X (2014) Subdivision of chatter-free regions and optimal cutting parameters based on vibration frequencies for peripheral milling process. Int J Mech Sci 83:172–183
3. Tobias SA (1977) Machine tool vibration. China Machine Press, Beijing
4. Smith S, Tlusty J (1990) Update on high-speed milling dynamics. Trans ASME J Eng Ind 112:142–149
5. Altintas Y, Budak E (1995) Analytical prediction of stability lobes in milling. Ann CIRP 44:357–362
6. Merdol SD, Altintas Y (2004) Multi frequency solution of chatter stability for low immersion milling. Trans ASME J Manuf Sci Eng 126:459–466
7. Faassen RPH, Wouw VDN, Nijimeijer H, Oosterling JAJ (2007) An improved tool path model including periodic delay for chatter prediction in milling. J Comput Nonlinear Dyn 2:167–179
8. Ding Y, Zhu LM, Zhang XJ, Ding H (2010) A full-discretization method for prediction of milling stability. Int J Mach Tools Manuf 50:502–509
9. Bayly PV, Halley JE, Mann BP, Davies MA (2003) Stability of interrupted cutting by temporal finite element analysis. Trans ASME J Manuf Sci Eng 125:220–225
10. Ding Y, Zhu LM, Zhang XJ, Ding H (2013) Stability analysis of milling via the differential quadrature method. Tans ASME J Manuf Sci Eng 135:044502–1–7
11. Totis G, Albertelli P, Sortino M, Monno M (2014) Efficient evaluation of process stability in milling with spindle speed variation by using the Chebyshev collocation method. J Sound Vib 333:646–668
12. Lehotzky D, Insperger T, Khasawneh F, Stepan G (2016) Spectral element method for stability analysis of milling processes with discontinuous time-periodicity. Int J Adv Manuf Technol. doi:10.1007/s00170-016-9044-z
13. Song QH, Ai X, Tang WX (2011) Prediction of simultaneous dynamic stability limit of time-variable parameters system in thin-walled workpiece high-speed milling processes. Int J Adv Manuf Technol 55:883–889
14. Luo M, Zhang DH, Wu BH, Zhou X (2011) Material removal process optimization for milling of flexible workpiece considering machining stability. Proc Inst Mech Eng B-J Eng Manuf 225:1263–1272
15. Budak E, Altintas Y (1998) Analytical prediction of chatter stability in milling—part II: application of the general formulation to common milling systems. Trans ASME J Dyn Syst 120:31–36
16. Ukar E, Campa FG, Sanchez JA, Rivero A (2005) The milling of airframe components with low rigidity: a general approach to avoid static and dynamic problems. Proc Inst Mech Eng B-J Eng Manuf 219:789–802
17. Bravo U, Altuzarra O, Lopez de Lacalle LN, Sanchez JA, Campa FJ (2005) Stability limits of milling considering the flexibility of the workpiece and the machine. Int J Mach Tools Manuf 45:1669–1680
18. Thevenot V, Arnaud L, Dessein G, Cazenave LG (2006) Integration of dynamic behaviour variations in the stability lobes method: 3D lobes construction and application to thin-walled structure milling. Int J Adv Manuf Technol 27:638–644
19. Thevenot V, Arnaud L, Dessein G, Cazenave LG (2006) Influence of material removal on the dynamic behavior of thin-walled structures. Mach Sci Technol 10(3):275–287
20. Song QH, Liu ZQ, Wan Y, Ju GG, Shi JH (2015) Application of Sherman-Morrison-Woodbury formulas in instantaneous dynamic of peripheral milling for thin-walled component. Int J Mech Sci 96–97:79–90
21. Seguy S, Dessein G, Arnaud L (2008) Surface roughness variation of thin wall milling related to modal interactions. Int J Mach Tools Manuf 48:261–274
22. Zhang XJ, Xiong CH, Ding Y (2011) A new solution for stability prediction in flexible part milling in intelligent robotics and applications. Sprnger-Verlag, Berlin Heidelberg, pp. 452–464
23. Zhang XJ, Xiong CH, Ding Y, Zhang XM (2010) Stability analysis in milling of thin-walled workpieces with emphasis on the structural effect. Proc Inst Mech Eng B-J Eng Manuf 224:589–608

24. Ilanko S, Bharathy GK (2012) Positive and negative penalty parameters in optimization subjected to continuous constraints. Comput Struct 108–109:83–92
25. Chakraverty S (2009) Vibration of plate: vibration basics for plates. CRC Press, Taylor & Francis Group, Boca Raton
26. Ilanko S, Monterrubio LE (2014) The Rayleigh-Ritz method for structural analysis. John Wiley & Sons, Inc., Hoboken
27. Monterrubio LE, Ilanbo S (2015) Proof of convergence for a set of admissible functions for the Rayleigh-Ritz analysis of beams and plates and shells of rectangular planform. Comput Struct 147:236–243
28. Richardson MH, Formenti DL (1982) Parameter estimation from frequency response measurements using rational fraction polynomials. Proc 1st Int Modal Anal Conf Orlando FL 1:167–186
29. Rao SS (2011) Mechanical vibration, 5th edn. Prentice Hall, Upper Saddle River
30. Song QH, Shi JH, Liu ZQ, Wan Y (2016) Dynamic analysis of rectangular thin plates of arbitrary boundary conditions under moving loads. Int J Mech Sci 117:16–29
31. Altintas Y (2012) Manufacturing automation: metal cutting mechanics, machine tool vibrations, and CNC design, 2nd edn. Cambridge University Press, London